



Research paper

Photocatalytic CO₂ conversion on highly ordered mesoporous materials: Comparisons of metal oxides and compound semiconductorsYoon Yun Lee^{a,1}, Han Sol Jung^{a,1}, Ji Man Kim^b, Yong Tae Kang^{a,*}^a School of Mechanical Engineering, Korea University, Seoul, 02841, Republic of Korea^b Department of Chemistry, Sungkyunkwan University, Suwon, 16419, Republic of Korea

ARTICLE INFO

Keywords:

CO₂ conversion
Mesoporous materials
Photocatalysts
Yield rates

ABSTRACT

In this study, the ordered mesoporous metal oxides (TiO₂ and SnO₂) and compound semiconductors (ZnS, ZnSe, CdS, and CdSe) are manufactured and they exhibit several micrometers (μm) of particle size, and high surface area of about 100 m²g⁻¹. Well-developed crystallinities are prepared via simple nano-replication method by using a 3-D bicontinuous cubic *Ia3d* meso-structured ordered mesoporous silica KIT-6 as a hard-template. The visible-light-driven photocatalytic CO₂ conversion into CH₄ is carried out in the presence of H₂O over various mesoporous materials. Prepared mesoporous materials show different light absorption behaviors and photocatalytic activities for conversion of CO₂. The mesoporous compound semiconductors show higher CO yield rates than the mesoporous metal oxides, while mesoporous metal oxides show higher CH₄ yield rates than the mesoporous compound semiconductors. Compared to the commercial TiO₂ material (P25, Degussa), the mesoporous metal oxides (TiO₂, SnO₂) show 9 to 10 times higher yields of CH₄ and 2 to 3 times higher yields of CO owing to their high surface area. Especially, the mesoporous ZnS shows the highest CH₄ yield rate (3.620 μmol g_{cat}⁻¹h⁻¹) and the mesoporous CdSe shows the highest CO yield rate (5.884 μmol g_{cat}⁻¹h⁻¹) out of all photocatalysts considered in the present study. Although mesoporous CdS and ZnSe have great visible light absorption properties, they show relatively low CH₄ yield rates.

1. Introduction

In recent, due to an increase in the energy demands caused by a population explosion, net CO₂ emission to atmospheres has dramatically increased by consumption of fossil fuels. Ultimately, in order to reduce the total net emission of CO₂, development of novel carbon capture and utilization (CCU) technology including capture, storage and conversion of CO₂ to fuels is highly required. Photocatalytic conversion of CO₂ is one of the most important technologies for reducing CO₂ emission, because no further thermal energy input is required in the system [1].

However, from the perspective of material science, still these technologies are hindered by significant limitations such as low photocatalytic activity. In the case of inorganic materials as a photocatalyst, band gap energy, band edge position and light absorption properties are critical factors, and also increment of active sites of photocatalyst is recommended for improving the photocatalytic activity [2–4]. By the absorption of light energy, electron hole pairs are generated in the photocatalyst particles, and electrons and holes migrate to the conduction band and valence band, respectively. Besides, if the conduction

band edge potential is higher than the redox potential, the photo-generated electrons in the mesoporous materials may convert CO₂ into other products [5,6]. To cope with, nano-structured materials such as TiO₂, Fe₂O₃, WO₃, ZnO, SnO₂, ZnS and CdS as effective photocatalysts have been investigated for environmental remediation because of their chemical stability and reasonable conductivity. In addition, porous materials has been studied to improve the photocatalytic activity for bulky molecules [4,7–11].

Especially nano-structured mesoporous materials, exhibiting well-defined mesopore sizes and nano-sized wall-thicknesses have some advantages as photocatalysts: (1) the high surface area which provides more active sites for photocatalytic reaction, (2) controllable mesopore sizes and connectivity that offer a short diffusion pathway for the reactants, and (3) shortening the transportation of electrons and holes into the surface of the materials by their nano-sized crystalline walls (usually < 10 nm) [12]. Accordingly, mesoporous materials with developed crystalline frameworks such as metal oxides and compound semiconductors have been extensively paid attention as photocatalysts for degradation of organic pollutants, water splitting, and environmental remediation. Especially, compound crystalline metal sulfides

* Corresponding author at: Room 309, Innovation Hall, 145 Anam-ro, Seongbuk-gu, Seoul 02841, Republic of Korea.

E-mail address: ytkang@korea.ac.kr (Y.T. Kang).¹ Y.Y. Lee and H. S. Jung share the first authorship of 50%, respectively.

and metal selenides are classified as compound semiconductors even when the considered oxides are semiconductors. However, due to the lack of suitable precursors and synthetic procedure, a major challenge for preparing high quality mesoporous compound semiconductor as photocatalysts is to find a suitable and facile preparation method [13]. There are only a few examples of mesoporous CdS, ZnS, CdSe and ZnSe with highly ordered *meso*-structures, and uniform pore sizes are prepared *via* nano-replication method, which is well-known for synthesizing ordered mesoporous material, using 3-D cubic *Ia3d* KIT-6 as a hard-template.

In the present study, highly ordered mesoporous materials with 3-D pore system, metal oxides of SnO₂ and TiO₂, and compound semiconductors of CdS, CdSe, ZnS and ZnSe, are synthesized *via* the nano-replication route. The obtained mesoporous materials, exhibiting ordered 3-D *meso*-structures with novel crystallinities, show high surface areas, large pore volume and outstanding photocatalytic performances. Afterwards, we compared the photocatalytic CO₂ conversion performances for the mesoporous metal oxides and compound semiconductors under the visible light irradiation.

2. Experiments

2.1. Synthesis of 3-D cubic *ia3d* mesoporous silica template KIT-6

Ordered mesoporous silica KIT-6 was prepared by previously reported method [14], which produced remarkably high surface areas and pore volumes combined with highly accessible and highly connected open porous networks. It was used as a hard-template for synthesis of mesoporous metal oxides and compound semiconductors in the present study. Pluronic® triblock copolymer P123 (EO₂₀PO₇₀EO₂₀, Aldrich, M_w = 5800) and tetraethyl orthosilicate (Si(OCH₂CH₃)₄, Samchun Chemical, 98%) were used as the structure-directing agent (SDA) and a silica source, respectively. Typically, 30 g of P123 polymer was dissolved in a mixture solution of 30 g of *n*-butanol (C₄H₉OH, anhydrous, Aldrich, 99%), 59 g of hydrochloric acid (HCl, Samchun Chemical, 35 ~ 37%) and 1085 g of doubly distilled water at room temperature. The P123 dissolved solution was kept at 35 °C water bath for 3 h under vigorous stirring to reach thermal equilibrium condition. After that, 64.5 g of TEOS was added to the solution, and stirred at 35 °C for 24 h. Subsequently, mixture solution was aged for 24 h at 100 °C for further reaction of silica source. The white powdered products were filtered, dried and washed with doubly distilled water. A structure-directing agent (P123) was removed by ethanol (C₂H₅OH, Samchun Chemical, 99.5%) extraction and calcination at 550 °C for 3 h.

2.2. Preparation of mesoporous photocatalysts

Mesoporous photocatalysts of TiO₂, SnO₂, ZnS, CdS, ZnSe and CdSe were prepared by nano-replication method which corresponded to simple impregnation and heat treatment using mesoporous KIT-6 as a hard-template [15–18]. To synthesize mesoporous TiO₂, 0.6 g of titanium(IV) ethoxide (Ti(OC₂H₅)₄, Aldrich, technical grade) was dissolved in 30 mL of doubly distilled water, and white precipitates were collected by centrifuge and decantation of supernatant. A collected white precipitate was dissolved in 0.8 g of hydrochloric acid to produce clear TiO₂ precursor, followed by impregnation into 1.0 g of KIT-6 silica template. This TiO₂ precursor/KIT-6 composite was dried at 160 °C for 10 min, and this process was repeated 9 times more for maximizing the amount of TiO₂ precursor within the mesopore of silica template. And then, the sample was dried at 100 °C for 24 h, and calcined at 450 °C for 3 h under ambient condition. Finally, KIT-6 silica template was almost completely removed by strong base (1 M NaOH aqueous solution) treatment, and white powder of TiO₂ was obtained followed by washing with doubly distilled water and acetone [15]. Mesoporous SnO₂ material was prepared by melting-infiltration assisted nano-replication method [16]. Firstly, 3.06 g of tin(II) chloride dihydrate (SnCl₂·2H₂O,

Aldrich, 98%) was heated to 110 °C in order to obtain liquid phase of precursors, and impregnated to 2.0 g of pre-heated KIT-6 silica template (aged at 100 °C for 1 h before mixed with tin-precursors) by vigorous shaking and aging at 80 °C for 12 h. The tin-precursor/KIT-6 composite was heated to 700 °C for 3 h under static air conditions, and treated with hydrofluoric acid (HF, 20 wt%) in order to remove silica template. Mesoporous ZnS, CdS, ZnSe, and CdSe were prepared with similar synthetic procedures each other. In order to prepare mesoporous ZnS and CdS, zinc sulfate heptahydrate (ZnSO₄·7H₂O, Aldrich, 99%) and cadmium sulfate 8/3-hydrate (3CdSO₄·8H₂O, Sigma-Aldrich, ACS reagent, ≥ 99.0%) were used as a single precursor. On the other hand, mesoporous ZnSe and CdSe were obtained by using external selenium source. In case of synthesis of mesoporous ZnSe and CdSe, zinc nitrate hexahydrate (Zn(NO₃)₂·6H₂O, Samchun Chemical, 98%), cadmium sulfate hydrate (Cd(NO₃)₂·4H₂O, Samchun Chemical, 98%) and selenium dioxide (SeO₂, Samchun Chemical, 99.8%) were used as precursor reagents. For synthesizing the mesoporous ZnS, CdS, ZnSe, and CdSe, precursor solutions were firstly prepared as follows: 3.80 g of ZnSO₄·7H₂O for ZnS; 2.28 g of 3CdSO₄·8H₂O for CdS; 1.89 g of Zn(NO₃)₂·6H₂O and 0.69 g of SeO₂ for ZnSe; 2.12 g of Cd(NO₃)₂·4H₂O and 0.76 g of SeO₂ for CdSe were dissolved in 3.0 g of doubly distilled water [17,18]. Precursor solutions were impregnated into mesopores of the KIT-6 silica template (3.0 g) *via* incipient-wetness method. After drying at 80 °C in an oven for 12 h, the composites were heated to 200 °C for 1 h for decomposition of metal salt precursors, and then reduced at 500 °C for 3 h under H₂ atmosphere. The KIT-6 silica template was removed by using 1 M NaOH aqueous solution as an etchant at room temperature, and after drying at 80 °C for 12 h under N₂ atmosphere in order to prevent surface oxidation of the material, the mesoporous ZnS, CdS, ZnSe, and CdSe were obtained.

2.3. Characterization

Powder X-ray diffraction (XRD) patterns of the materials were characterized in reflection mode using a Rigaku Ultima IV equipped with Cu K_α (λ = 1.54 Å) at 40 kV and 30 mA N₂-sorption isotherms were obtained by Micromeritics Tristar II series at liquid temperature of N₂. All of the materials were dried under vacuum at 100 °C for 24 h in order to remove extra gas molecules before the measurement. Scanning electron microscopy (SEM) images were taken using a JEOL JSM-7100F FE-SEM operating at an accelerating voltage of 15 kV. Transmission electron microscopy (TEM) images were obtained using a JEOL JEM 3010 at an acceleration voltage of 300 kV.

2.4. Photocatalytic conversion of CO₂

Photocatalytic conversion of CO₂ is occurred in a tubular glass reactor. The closed photocatalytic CO₂ conversion reactor system was designed as shown Fig. 1. In this system, CO₂ with high purity (99.99%), controlled by a mass flow controller (TN 280/TN 380 series, Celerity), was injected into a suspension containing photocatalyst particles and DI water (Milli-Q® Integral, Mili-pore). Each photocatalyst (25 mg) was dispersed in DI water (200 mL) by using magnetic stirrer (400 rpm). The optimal concentration of photocatalyst was controlled by the same method as reported by Salaices et al. [19]. A 300 W Xe lamp (XLS-300-OFR, Spectro) was used as a UV-vis light source, and the suspension was irradiated with > 420 nm IR-Cutoff filtered light. A cooling water jacket was installed outside of the photo-reactor to prevent a temperature rise, and the temperature was maintained at 20 °C. In the present experiment, gaseous samples were analyzed by a gas chromatography focusing on the gas products [20,21]. For example, Teramura et al. [20] conducted photocatalytic reduction of CO₂, which was carried out in a closed circulating system connected to a vacuum line, with a quartz glass ceiling for illumination. The synthesized LDH (100 mg) was dispersed in water (4 mL). CO₂ (500 mmol), purified by vacuum distillation at liquid-N₂ temperature, was introduced into the

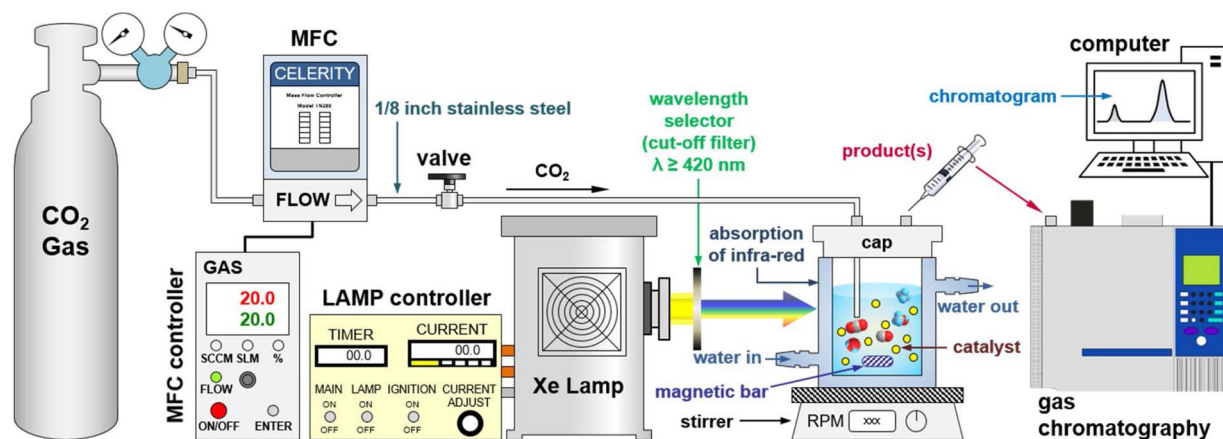


Fig. 1. Experimental setup for photocatalytic conversion of CO₂ with H₂O.

reactor and irradiated by a 200W Hg-Xe lamp (San-Ei Electric Co., Ltd., UVF-204S Type B) equipped with fiber optics, a collective lens, and a mirror. They focused on the gas product including CO and O₂ since they only used the gas chromatography for product detection. Furthermore, Dilla et al. [21] investigated photocatalytic CO₂ reduction on TiO₂ P25 under continuous flow conditions with gas chromatography to detect CH₄ as a main product. In the present experiments, the concentrations of CO and CH₄ from the photo-reactor were measured by a gas-chromatography (YL-6500 GC System, Young Lin Instrument) equipped with a 30 m × 0.530 mm × 3.00 μm PLOT capillary columns (Agilent Technologies) of which stationary phases were DB-624 and GS-Carbonplot. A thermal conductivity detector (TCD) and a flame ionization detector (FID) use He as a carrier gas. Prior to each photocatalytic CO₂ conversion reaction, the reactor was purged with the CO₂ at a flow rate of 20 mL/min for 30 min on dark room to reach the sorption equilibrium of CO₂ on the surface of photocatalyst particles. Afterward, the light source was turned on and the concentrations of produced gases were recorded as a function of irradiation time for 3 h when some of the photocatalysts (CdSe, ZnSe) finished CO₂ conversion reaction to CO. Each experiment was conducted at least three times independently, and the yields of CH₄ and CO were plotted with error bars, and the corresponding average product yield rates were obtained for each photocatalyst. Also, recycling tests were conducted with the used photocatalysts after being removed from the reactor followed by drying photocatalysts at 100 °C for 12 h. Then, the recycled photocatalysts were placed back in the reactor and photocatalytic conversion tests were conducted.

3. Results and discussion

3.1. Characteristics of mesoporous photocatalysts

Fig. 2A shows the low-angle XRD patterns for each mesoporous metal oxide and compound semiconductor and Fig. S1 (a) shows the low-angle XRD pattern of KIT-6 silica template. All of the replicated mesoporous materials show similar diffraction patterns, and compared to the low-angle XRD pattern of KIT-6 silica template, a new peak which corresponds to the (110) reflection plane appeared in low angle region ($2\theta < 0.5^\circ$). In addition, except the (211) peak, other diffraction peaks of (220), (420) and (332) planes were disappeared after silica template removal. It represents the *meso*-phase transformation from cubic *Ia3d* to tetragonal *I4₁/a* or lower symmetry by the mesoporous metal oxides and compound semiconductors during the silica template etching. Typically, this *meso*-structure transition occurred in the case of crystalline frameworks formed in only one of two chiral pore channel systems of KIT-6 silica [22].

Wide-angle XRD patterns of the mesoporous metal oxides and

compound semiconductors are quite different from each other as depicted in Fig. 2B, and all the replicated materials show broad peaks because the crystalline frameworks are formed within a confined small mesopores of silica template. As shown in Fig. 2B (a), mesoporous SnO₂ exhibits tetragonal rutile structure with a space group of *P4₂/mmm*, and the corresponding lattice parameters ($a = 4.746 \text{ \AA}$, $c = 3.189 \text{ \AA}$) are closely matched with the values given in the JCPDS card (#21-1250, $a = 4.738 \text{ \AA}$, $c = 3.188 \text{ \AA}$). Mesoporous TiO₂ show crystal structure of tetragonal anatase (*I4₁/amd*, JCPDS #01-1292) phase as depicted in Fig. 2B (b). The corresponding lattice parameters for mesoporous TiO₂ ($a = 3.760 \text{ \AA}$, $c = 9.370 \text{ \AA}$) are slightly different from the given values in JCPDS card (#01-0562, $a = 3.730.3 \text{ \AA}$, $c = 9.370 \text{ \AA}$). This is because the rutile phase is mixed within the crystal structure of mesoporous TiO₂. Mesoporous CdS and CdSe (Fig. 2B c, d) have hexagonal wurtzite crystal phase (*P6₃mc*, JCPDS #77-2306 for CdS; #08-0459 for CdSe), and the corresponding lattice parameters calculated from the XRD patterns ($a = 4.135 \text{ \AA}$, $c = 6.713 \text{ \AA}$ for CdS; $a = 4.295 \text{ \AA}$, $c = 7.011 \text{ \AA}$ for CdSe) are matched well with the reference values ($a = 4.136 \text{ \AA}$, $c = 6.713 \text{ \AA}$ in #77-2306 CdS; $a = 4.299 \text{ \AA}$, $c = 7.010 \text{ \AA}$ in #08-0459 CdSe). In contrast, Zn-based mesoporous materials (ZnS and ZnSe), exhibit cubic zinc blende structure with a space group of *F-43m* as shown in Fig. 2B (e, f). The corresponding lattice parameters of mesoporous ZnS ($a = 5.403 \text{ \AA}$) and ZnSe ($a = 5.667 \text{ \AA}$) are also totally same as the given values in the reference JCPDS cards ($a = 5.404 \text{ \AA}$ in #65-5476 ZnS; $a = 5.667 \text{ \AA}$ in #05-0522 ZnSe). In addition, as depicted in Fig. 2B (c, d) and (e, f), the mesoporous CdS, CdSe and ZnS, ZnSe have similar diffraction patterns each other, respectively, and the diffraction peak positions are shifted to lower 2θ with increases of counter anion size in crystal structures (S²⁻ in crystal 170 pm; Se²⁻ in crystal 184 pm).

The porosities of the mesoporous materials were analyzed by the N₂-sorption isotherm technique. The N₂-sorption isotherms and pore size distributions of the synthesized KIT-6 template are shown in Fig. S1 (b). As shown in Fig. 3A(a–f), all of the materials present typical type-IV with a hysteresis loop, which is the specific characteristics of the mesoporous materials. However, mesoporous SnO₂ and TiO₂ have two capillary condensation regions at adsorption branches in N₂-sorption isotherms (Fig. 3A a, b), which correspond to dual pore systems. The mesoporous SnO₂ (Fig. 3B a, 3.3 and 18 nm) and TiO₂ (Fig. 3B b, 6.1 and 18 nm) exhibit dual porous structures which are caused by silica frameworks (smaller pore) after the replication process, and *meso*-phase transformation (larger pore) as discussed in low-angle XRD patterns. In contrast, as presented in Fig. 3B (c–f), mesoporous compound semiconductors show only one pore size distributions of ca. 16 ~ 18 nm because the crystalline frameworks of materials are formed only in one of two chiral pore channels of the KIT-6 silica template. This pore size distribution curves are strongly matched with the appearance of new diffraction peaks of (110) reflection plane in low-angle XRD patterns in Fig. 2A (c–f), which are originated by the structural transition of cubic

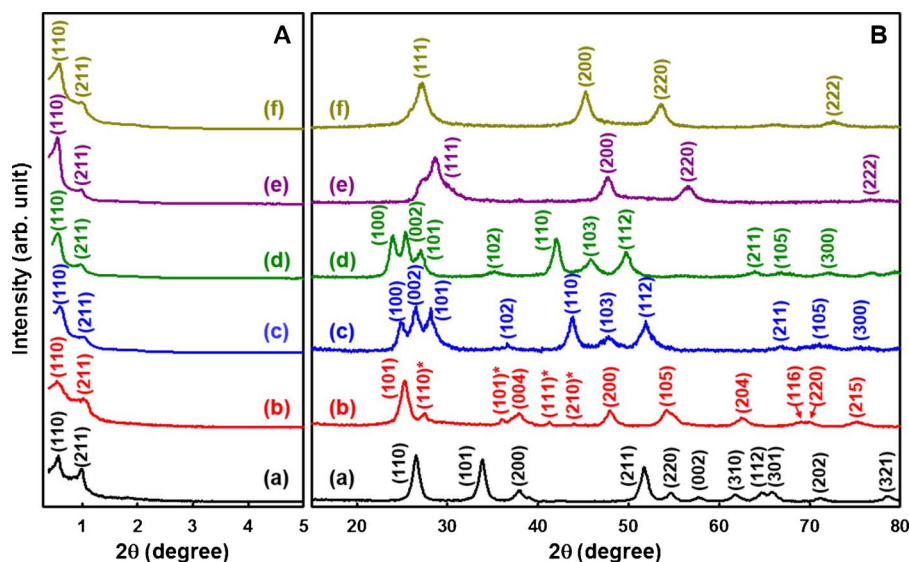


Fig. 2. (A) Low- and (B) wide-angle XRD patterns of the mesoporous (a) SnO₂, (b) TiO₂, (c) CdS, (d) CdSe, (e) ZnS, and (f) ZnSe. (*Rutile phase of TiO₂).

Ia3d to tetragonal *I4₁/a* or lower symmetry. Specific BET surface areas, total pore volumes, pore diameters of mesoporous materials are summarized in Table 1. Specific BET surface areas were calculated from the adsorption branches in the range of $p/p_0 = 0.05 \sim 0.20$ of N₂-sorption isotherms. Total pore volumes were obtained from N₂-sorption isotherms at $p/p_0 = 0.99$. Also, pore diameters of the materials calculated from the adsorption branches of the N₂-sorption isotherms by using the BJH method.

The optical properties of the mesoporous materials are characterized by diffuse-reflectance UV–visible spectroscopy, and the resulting spectrums are shown in Fig. 4A. Band gap energies are estimated from the Kubelka-Munk plots of the mesoporous materials, which are shown in Fig. 4B. Also, band gap energy of P25 material is estimated about 3.50 eV, which is shown in Fig. S2 (a), (b). Other literature also provided the band gap energy of P25 material of 3.50 eV [23,24]. Moreover, the mesoporous SnO₂, TiO₂ and ZnS absorb only partial portion of UV light below about 400 nm (see Fig. 4A (a, b and e)), corresponding to the wide band gap energies. In contrast, mesoporous CdS, CdSe and ZnSe strongly absorb visible light range as depicted in Fig. 4A (c, d and f) owing to their small band gap energies. As shown in Fig. 4B, the Kubelka-Munk plots of the mesoporous materials calculated by the

Table 1

Physical and optical properties of mesoporous materials.

Material	S_{BET} (m ² g ^{−1}) ^a	V_{total} (cm ³ g ^{−1}) ^b	D_p (nm) ^c	E_g (eV) ^d
meso-SnO ₂	97.0	0.22	3.3 & 18	3.63
meso-TiO ₂	209.0	0.75	6.1 & 18	3.62
meso-CdS	81.2	0.67	18.2	2.43
meso-CdSe	93.1	0.43	16.5	1.86
meso-ZnS	127.1	0.82	16.6	3.64
meso-ZnSe	116.3	0.54	19.7	2.70

^a Specific BET surface areas were calculated from the adsorption branches in the range of $p/p_0 = 0.05 \sim 0.20$ of N₂-sorption isotherms.

^b Total pore volumes were obtained from N₂-sorption isotherms at $p/p_0 = 0.99$.

^c Pore diameters of the materials calculated from the adsorption branches of the N₂-sorption isotherms by using BJH method.

^d Band gap energies estimated from the Kubelka-Munk plots in Fig. 4B.

following Eq. (1) from the diffuse reflectance UV–vis spectra in Fig. 4A:

$$F(R) = \frac{(1 - R)^2}{2R} \quad (1)$$

where R is the reflectance [25,26]. The estimated band gap energies of

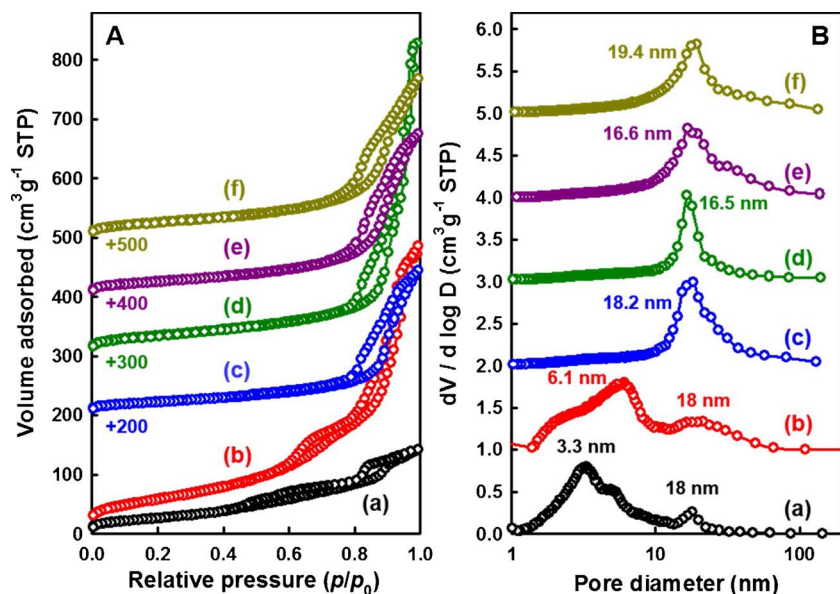


Fig. 3. (A) N₂-sorption isotherms and (B) BJH pore size distributions of the mesoporous (a) SnO₂, (b) TiO₂, (c) CdS, (d) CdSe, (e) ZnS, and (f) ZnSe.

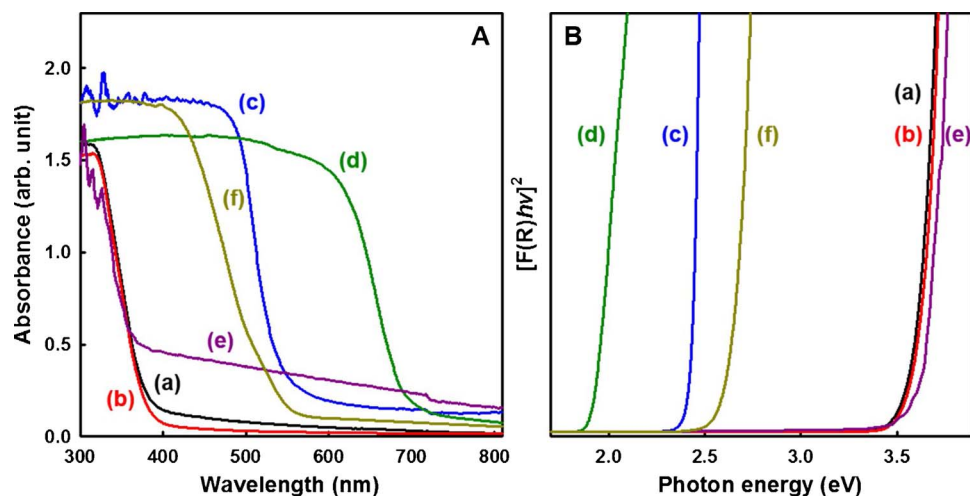


Fig. 4. Diffuse reflectance UV-vis spectra and (B) Kubelka-Munk plots of the mesoporous (a) SnO_2 , (b) TiO_2 , (c) CdS , (d) CdSe , (e) ZnS , and (f) ZnSe .

mesoporous SnO_2 , TiO_2 , CdS , CdSe , ZnS , and ZnSe from the Kubelka-Munk plots are 3.63, 3.62, 2.43, 1.86, 3.64, and 2.70 eV, respectively. These values are larger than those of bulk TiO_2 (3.20 eV), CdS (2.42 eV), CdSe (1.75 eV), ZnS (3.50 eV), and ZnSe (2.43 eV) except SnO_2 (3.81 eV). This band gap widening phenomenon is related to the quantum confinement effect of nano-sized frameworks of mesoporous materials which can also be confirmed by the wide-angle XRD patterns in Fig. 2B. [18]. The bandgap energies are summarized in Table 1.

The overall particle morphologies and several micrometers (μm) of particle size of mesoporous materials with ordered *meso*-structures are shown in Fig. 5A. Because the same mesoporous silica KIT-6 is used as a hard-template, the overall particle morphologies of the replicated mesoporous materials are very similar to each other. The developed crystalline frameworks and highly ordered *meso*-structures with uniform pore sizes of the replicated mesoporous materials are presented in the TEM (Fig. 5B) and HR-TEM (Fig. 5C) images, respectively.

3.2. Photocatalytic conversion of CO_2

The photocatalytic conversion of CO_2 with mesoporous metal oxides and compound semiconductors under light irradiation were performed by using a close-reactor system as shown in Fig. 1. In order to achieve the high yields of CO and CH_4 , a photocatalyst should have outstanding light absorption property and high surface area. As shown in Table 1, the mesoporous materials prepared in this study have extremely high surface area about $100 \text{ m}^2/\text{g}$ or higher, and outstanding light absorption properties from UV to visible light range, which are suitable for photo-conversion of CO_2 into CO and CH_4 . To compare the photocatalytic activity of the commercial TiO_2 with that of the mesoporous metal oxides (TiO_2 , SnO_2), P25 (Degussa) was also used as a reference photocatalyst for conversion of CO_2 . Figs. 6 and 7 show the yields and the average yield rates of CH_4 for each photocatalyst, respectively, and Figs. 8 and 9 do the yields and the average yield rates of CO ,

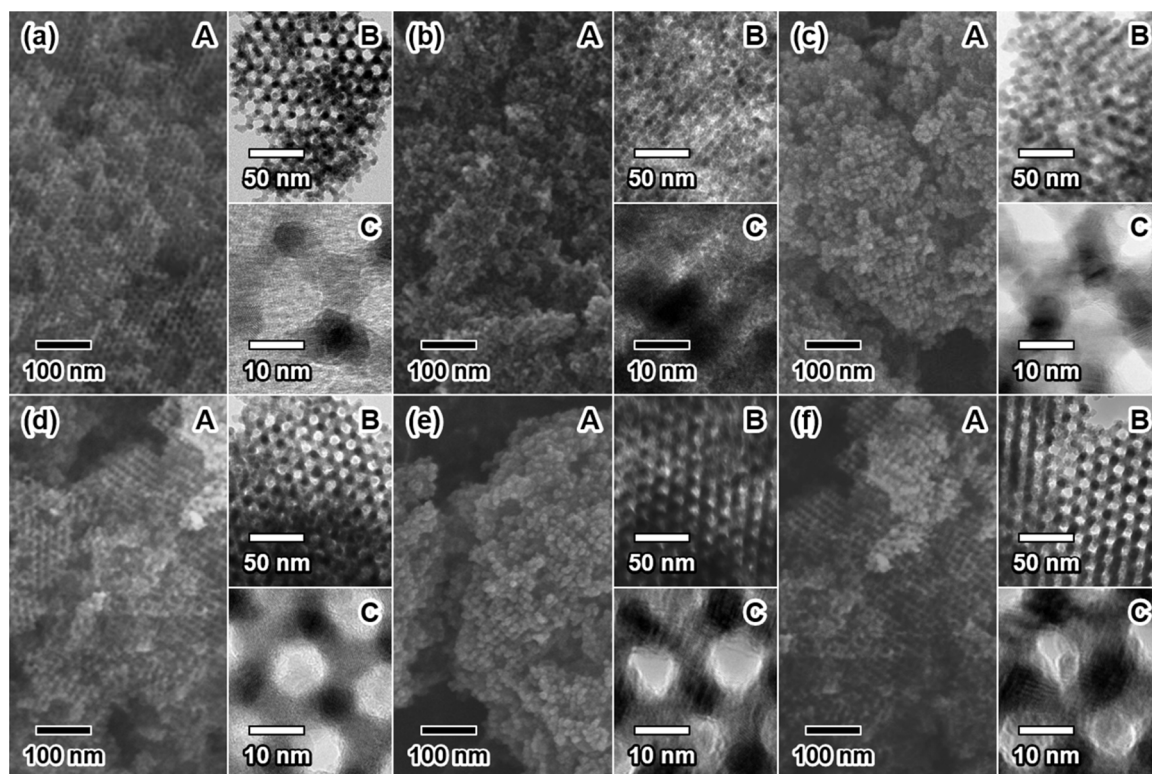


Fig. 5. (A) SEM, (B) TEM and (C) HR-TEM images of the mesoporous (a) SnO_2 , (b) TiO_2 , (c) CdS , (d) CdSe , (e) ZnS , and (f) ZnSe .

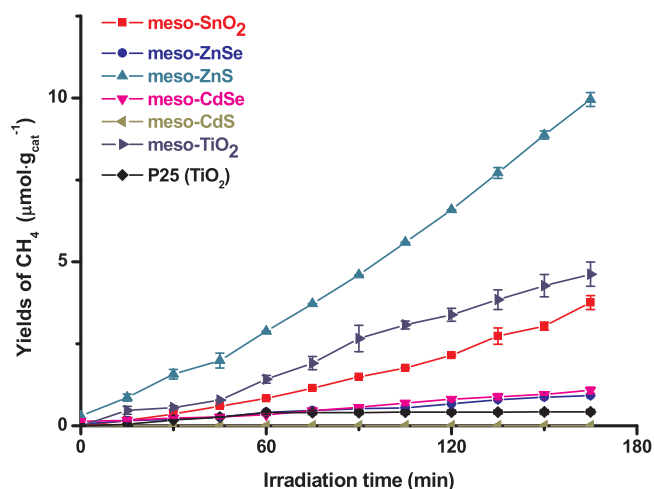


Fig. 6. Yields of CH₄ by using various photocatalysts, P25 (commercial TiO₂, Degussa, anatase + rutile phases) and mesoporous materials (TiO₂, SnO₂, CdS, CdSe, ZnS and ZnSe).

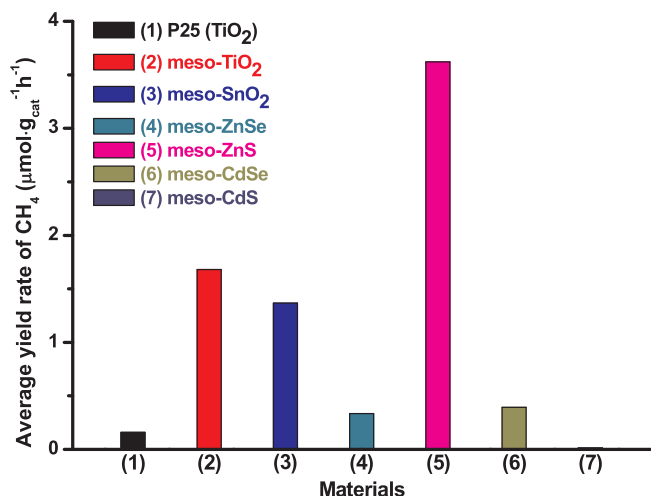


Fig. 7. Average yield rate of CH₄ by using various photocatalysts, P25 (commercial TiO₂, Degussa, anatase + rutile phases) and mesoporous materials (TiO₂, SnO₂, CdS, CdSe, ZnS and ZnSe).

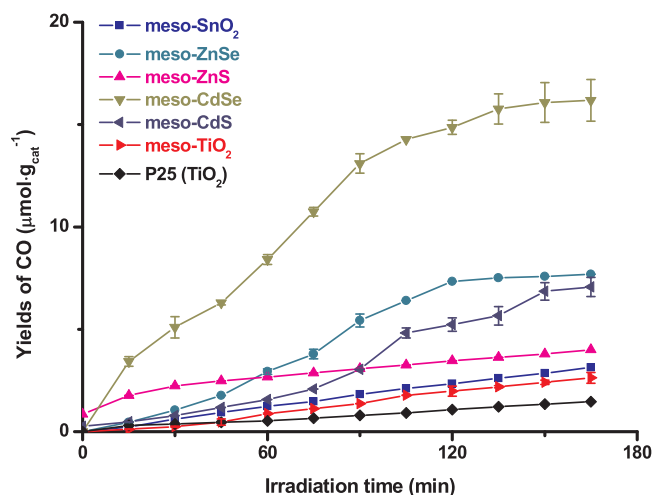


Fig. 8. Yields of CO by using various photocatalysts, P25 (commercial TiO₂, Degussa, anatase + rutile phases) and mesoporous materials (TiO₂, SnO₂, CdS, CdSe, ZnS and ZnSe).

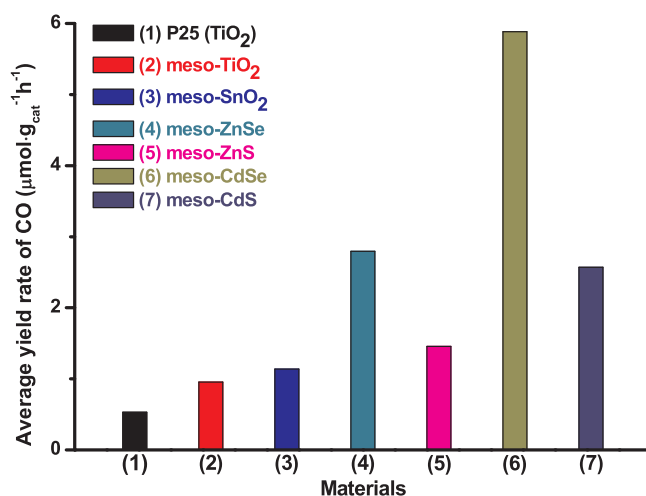


Fig. 9. Average yield rate of CO by using various photocatalysts, P25 (commercial TiO₂, Degussa, anatase + rutile phases) and mesoporous materials (TiO₂, SnO₂, CdS, CdSe, ZnS and ZnSe).

respectively. As shown in Figs. 6 and 8, it can be found that the mesoporous metal oxides (TiO₂, SnO₂) produce 9–10 times higher yields of CH₄ and 2–3 times higher yields of CO owing to their high surface area. As shown in Figs. 7 and 9, the yield rates of the commercial P25 are only 0.159 μmol g_{cat}⁻¹h⁻¹ of CH₄ and 0.531 μmol g_{cat}⁻¹h⁻¹ of CO after 165 min of light irradiation time. As depicted in Fig. 4A (a) and (b), owing to its poor light absorption property and low surface area, relatively small amounts of products are obtained by the reaction [27]. The mesoporous SnO₂ and TiO₂ show very similar light absorption properties, and their band gap energies (3.63 eV for SnO₂; 3.62 eV for TiO₂) are also very close to each other. The framework thickness of anatase TiO₂ may decrease with increasing the amount of silica, and this can cause the band gap widening phenomenon due to the quantum confinement effect. This phenomenon of the band gap energy change by the control of loading amount of TiO₂ on the mesoporous silica was also confirmed by Araujo et al. [28]. In the case of mesoporous TiO₂, the yield rates are 1.681 μmol g_{cat}⁻¹h⁻¹ of CH₄ and 0.956 μmol g_{cat}⁻¹h⁻¹ of CO. The yield rates of each product are much higher than those of P25 as shown in Fig. 2B (b). Because the mesoporous TiO₂ exhibits much higher surface area of 209 m²/g than P25 (56 m²/g) and/or TiO₂ NPs (45–55 m²/g), this CO₂ conversion enhancement effect is strongly associated with surface area enhancement [29]. Similarly, the yield rates of the mesoporous SnO₂ are 1.367 μmol g_{cat}⁻¹h⁻¹ of CH₄ and 1.139 μmol g_{cat}⁻¹h⁻¹ of CO. This result reveals that the surface area and the light absorption properties are closely related to the yield rate of products.

The mesoporous SnO₂ and TiO₂ almost cannot absorb the visible light in this condition. However, in many cases, the defect sites on the crystalline frameworks of metal oxides cause the scattering of light on the surface of photocatalyst particles, and it excites electrons from valence band to conduction band with a small portion. By this phenomenon, the mesoporous SnO₂ and TiO₂ also exhibit photocatalytic activities with low conversion efficiency in this experiment condition [30]. Furthermore, when the KIT-6 and TiO₂ coexist, the photic scattering effect is increased by the pore structure of the amorphous silica framework.

Besides the mesoporous metal oxides, the compound semiconductors of CdS, CdSe, ZnS and ZnSe with an ordered mesoporous structure were also investigated as photocatalysts for CO₂ conversion. As shown in Fig. 4A (a) and (b), synthesized compound semiconductors have great visible light absorption properties. The yield rates of the mesoporous CdS are almost 0 μmol g_{cat}⁻¹h⁻¹ of CH₄, and 2.571 μmol g_{cat}⁻¹h⁻¹ of CO. This result reveals that CdS is a good photocatalyst for selective formation of HCOOH or CO by conversion of

CO₂, and only very small amount of CH₄ might be produced by photo-conversion of CO₂ due to its conduction band edge position [31–33]. The mesoporous CdSe produces the highest CO yield rate (5.884 μmol g_{cat}⁻¹h⁻¹) out of all photocatalysts considered in the present study, while it shows relatively low yield rate of CH₄ (0.393 μmol g_{cat}⁻¹h⁻¹). The reason may be attributed to a smaller bandgap than other mesoporous materials that allow photoconversion of CO₂ with visible light [34]. Mesoporous ZnS shows the highest CH₄ yield rate (3.620 μmol g_{cat}⁻¹h⁻¹) out of all photocatalysts considered in the present study, and it produces 1.456 μmol g_{cat}⁻¹h⁻¹ of CO. The yield rates of mesoporous ZnSe are 0.335 μmol g_{cat}⁻¹h⁻¹ of CH₄ and 2.793 μmol g_{cat}⁻¹h⁻¹ of CO. Although the mesoporous ZnSe has great light absorption ability and photocatalytic activity, the yield rates of CH₄ and CO are lower than those of ZnS. This result explains why ZnS is commonly designed as a photocatalyst for CO₂ reduction, while ZnSe is rarely studied as a photocatalyst due to its high photoluminescence property [35–37]. Therefore, it can be said that not only light absorption property but also bandgap energy, band edge position and PL property affect the yield rates of each product. As shown in Fig. 8, after 150 min, in the cases of mesoporous CdSe and ZnSe produced only small amount of additional CO due to the following reasons: 1) decrease of the adsorption power of the catalysts and the saturation of adsorption sites on the surface; 2) photo-generated electrons in conduction band are quickly recombined with holes in valence band. [37,38]. This result implies that the hole scavenger is required for optimum amounts of ions to be on the surface in order to maximize electrons and holes transferred [39]. Also, the photocatalytic conversion experiments are conducted again with the used photocatalysts after being removed from the reactor followed by drying photocatalysts at 100 °C for 12 h, and it produced a slightly reduced yield, less than 10% loss. These results indicate that the photocatalyst is largely regenerated during the regeneration process due to desorption of the products from its surface.

4. Conclusions

In this study, highly ordered metal oxides and compound semiconductors were prepared via nano-replication method with unique physicochemical and optical properties. The synthesized materials show high surface area, ordered *meso*-structures, and outstanding light absorption properties. Afterwards, the photocatalytic conversion of CO₂ into CH₄ and CO was tested under the visible light irradiation by using mesoporous metal oxides and compound semiconductors.

Compared to the commercial TiO₂ material (P25, Degussa), the mesoporous metal oxides (TiO₂, SnO₂) show 9–10 times higher yields of CH₄ owing to their high surface area and 2–3 times higher yields of CO. The mesoporous compound semiconductors exhibit improved visible light absorption properties. Besides, the bandgaps of mesoporous ZnSe, CdSe and CdS are much smaller than those of the mesoporous metal oxides. By these reasons, the mesoporous compound semiconductors show higher CH₄ and CO yield rates than the mesoporous metal oxides. Especially, the mesoporous ZnS shows the highest CH₄ yield rate (3.620 μmol g_{cat}⁻¹h⁻¹) out of all photocatalysts considered in the present study while the mesoporous CdSe shows the highest CO yield rate (5.884 μmol g_{cat}⁻¹h⁻¹). Although mesoporous CdS and ZnSe have great visible light absorption properties, they show relatively low CH₄ yield rates, which might be related to following reasons: 1) CdS favors the formation of HCOOH and CO rather than CH₄ due to its surface property; 2) Although ZnSe have good visible light absorption property, it exhibits great PL property simultaneously, and therefore the photocatalytic activity is reduced. Moreover, after 150 min, mesoporous CdSe and ZnSe produces only small amount of additional CO due to the decrease of the adsorption power of the particles and saturation of the adsorption sites on the surface.

Acknowledgements

This work was supported by the National Research Foundation of Korea(NRF) grant funded by the Korea government(MSIP) (No. NRF-2016R1A2B3007577) and by the Human Resources Program in Energy Technology of the Korea Institute of Energy Technology Evaluation.

Appendix A. Supplementary data

Supplementary data associated with this article can be found, in the online version, at <http://dx.doi.org/10.1016/j.apcatb.2017.10.068>.

References

- [1] W. Tu, Y. Zhou, Z. Zou, Photocatalytic conversion of CO₂ into renewable hydrocarbon fuels: state-of-the-Art accomplishment, challenges, and prospects, *Adv. Mater.* 26 (2014) 4607–4626.
- [2] R.M. Navarro Yerga, M.C. Álvarez Galván, F. Del Valle, J.A. Villoria de la Mano, J.L. Fierro, Water splitting on semiconductor catalysts under Visible Light irradiation, *ChemSusChem* 2 (2009) 471–485.
- [3] S.B. Rawal, S. Bera, D. Lee, D.-J. Jang, W.I. Lee, Design of visible-light photocatalysts by coupling of narrow bandgap semiconductors and TiO₂: effect of their relative energy band positions on the photocatalytic efficiency, *Catal. Sci. Technol.* 3 (2013) 1822–1830.
- [4] N. Linares, A.M. Silvestre-Albero, E. Serrano, J. Silvestre-Albero, J. García-Martínez, Mesoporous materials for clean energy technologies, *Chem. Soc. Rev.* 43 (2014) 7681–7717.
- [5] M. Setvin, X. Hao, B. Daniel, J. Pavelec, Z. Novotny, G.S. Parkinson, et al., Charge trapping at the step edges of TiO₂ anatase (101), *Angew. Chem. Int. Ed.* 53 (2014) 4714–4716.
- [6] M.F. Ehsan, M.N. Ashiq, T. He, Hollow and mesoporous ZnTe microspheres: synthesis and visible-light photocatalytic reduction of carbon dioxide into methane, *RSC Adv.* 5 (2015) 6186–6194.
- [7] M.N. Chong, B. Jin, C.W. Chow, C. Saint, Recent developments in photocatalytic water treatment technology: a review, *Water Res.* 44 (2010) 2997–3027.
- [8] H. Zheng, J.Z. Ou, M.S. Strano, R.B. Kaner, A. Mitchell, K. Kalantar-zadeh, Nanostructured tungsten oxide—properties, synthesis, and applications, *Adv. Funct. Mater.* 21 (2011) 2175–2196.
- [9] M. Pelaez, N.T. Nolan, S.C. Pillai, M.K. Seery, P. Falaras, A.G. Kontos, et al., A review on the visible light active titanium dioxide photocatalysts for environmental applications, *Appl. Catal. B: Environ.* 125 (2012) 331–349.
- [10] H. Tong, S. Ouyang, Y. Bi, N. Umezawa, M. Oshikiri, J. Ye, Nano-photocatalytic materials: possibilities and challenges, *Adv. Mater.* 24 (2012) 229–251.
- [11] K.K.R. KSR, Zinc oxide based photocatalysis: tailoring surface-bulk structure and related interfacial charge carrier dynamics for better environmental applications, *RSC Adv.* 5 (2015) 3306–3351.
- [12] A.A. Ismail, D.W. Bahnemann, Mesoporous titania photocatalysts: preparation: characterization and reaction mechanisms, *J. Mater. Chem.* 21 (2011) 11686–11707.
- [13] Y. Shi, Y. Wan, D. Zhao, Ordered mesoporous non-oxide materials, *Chem. Soc. Rev.* 40 (2011) 3854–3878.
- [14] F. Kleitz, S.H. Choi, R. Ryoo, Cubic Ia3d large mesoporous silica: synthesis and replication to platinum nanowires, carbon nanorods and carbon nanotubes, *Chem. Commun.* (2003) 2136–2137.
- [15] S.S. Kim, H.I. Lee, J.K. Shon, J.Y. Hur, M.S. Kang, S.S. Park, et al., Preparation of highly ordered mesoporous TiO₂ materials with crystalline framework from different mesostructured silica templates via nanoreplication, *Chem. Lett.* 37 (2008) 140–141.
- [16] J.K. Shon, S.S. Kong, Y.S. Kim, J.-H. Lee, W.K. Park, S.C. Park, et al., Solvent-free infiltration method for mesoporous SnO₂ using mesoporous silica templates, *Microporous Mesoporous Mater.* 120 (2009) 441–446.
- [17] Y.Y. Lee, S. Bae, J.M. Kim, 3-D ordered mesoporous Cd x zn1-x S ternary compound semiconductors with controlled band gap energy, *J. Nanosci. Nanotechnol.* 14 (2014) 9033–9036.
- [18] Y.Y. Lee, J.K. Shon, S. Bae, X. Jin, Y.J. Choi, S.S. Kwon, et al., Highly ordered mesoporous Cd_xZn_{1-x}Se ternary compound semiconductors with controlled band gap energies, *New J. Chem.* 38 (2014) 3729–3736.
- [19] M. Salaices, B. Serrano, H. De Lasa, Experimental evaluation of photon absorption in an aqueous TiO₂ slurry reactor, *Chem. Eng. J.* 90 (2002) 219–229.
- [20] K. Teramura, S. Iguchi, Y. Mizuno, T. Shishido, T. Tanaka, Photocatalytic conversion of CO₂ in water over layered double hydroxides, *Angew. Chem.* 124 (2012) 8132–8135.
- [21] M. Dilla, R. Schlögl, J. Strunk, Photocatalytic CO₂ reduction under continuous flow HighPurity conditions: quantitative evaluation of CH₄ formation in the SteadyState, *ChemCatChem* . 9 (2017) 696–704.
- [22] Y. Doi, A. Takai, Y. Sakamoto, O. Terasaki, Y. Yamauchi, K. Kuroda, Tailored synthesis of mesoporous platinum replicas using double gyroid mesoporous silica (KIT-6) with different pore diameters via vapor infiltration of a reducing agent, *Chem. Commun.* 46 (2010) 6365–6367.
- [23] G. Colon, M. Hidalgo, J. Navio, Photocatalytic deactivation of commercial TiO₂ samples during simultaneous photoreduction of Cr (VI) and photooxidation of

- salicylic acid, *J. Photochem. Photobiol. A: Chem.* 138 (2001) 79–85.
- [24] G. Colón, M. Hidalgo, J. Navio, Influence of carboxylic acid on the photocatalytic reduction of Cr (VI) using commercial TiO₂, *Langmuir* 17 (2001) 7174–7177.
- [25] P. Kubelka, F. MUNK, Ein Beitrag zur Optik der farbanstriche, *Z. Tech. Phys.* 12 (1931) 593.
- [26] P. Kubelka, New contributions to the optics of intensely light-scattering materials. Part I, *JOSA* 38 (1948) 448.
- [27] D. Wodka, R.P. Socha, E. Bielańska, M. Elżbieciak-Wodka, P. Nowak, P. Warszyński, Photocatalytic activity of titanium dioxide modified by Fe₂O₃ nanoparticles, *Appl. Surf. Sci.* 319 (2014) 173–180.
- [28] M. Araujo, L. Silva, J. Sczancoski, M. Orlandi, E. Longo, A. Santos, et al., Anatase TiO₂ nanocrystals anchored at inside of SBA-15 mesopores and their optical behavior, *Appl. Surf. Sci.* 389 (2016) 1137–1147.
- [29] K.J.A. Raj, B. Viswanathan, Effect of surface area: pore volume and particle size of P25 titania on the phase transformation of anatase to rutile, *Indian J. Chem. A* 48 (2009) 1378–1382.
- [30] S. Munnix, M. Schmeits, Electronic structure of oxygen vacancies on TiO₂ (110) and SnO₂ (110) surfaces, *J. Vac. Sci. Technol. A Vac. Surf. Films* 5 (1987) 910–913.
- [31] H. Inoue, R. Nakamura, H. Yoneyama, Effect of charged conditions of stabilizers for cadmium sulfide microcrystalline photocatalysts on photoreduction of carbon dioxide, *Chem. Lett.* (1994) 1227–1230.
- [32] H. Fujiwara, H. Hosokawa, K. Murakoshi, Y. Wada, S. Yanagida, T. Okada, et al., Effect of surface structures on photocatalytic CO₂ reduction using quantized CdS nanocrystallites, *J. Phys. Chem. B* 101 (1997) 8270–8278.
- [33] B.-J. Liu, T. Torimoto, H. Yoneyama, Photocatalytic reduction of CO₂ using surface-modified CdS photocatalysts in organic solvents, *J. Photochem. Photobiol. A: Chem.* 113 (1998) 93–97.
- [34] W. Lin, H. Frei, Photochemical CO₂ splitting by metal-to-metal charge-transfer excitation in mesoporous ZrCu(I)-MCM-41 silicate sieve, *J. Am. Chem. Soc.* 127 (2005) 1610–1611.
- [35] H. Fujiwara, H. Hosokawa, K. Murakoshi, Y. Wada, S. Yanagida, Surface characteristics of ZnS nanocrystallites relating to their photocatalysis for CO₂ reduction, *Langmuir* 14 (1998) 5154–5159.
- [36] J. Chen, F. Xin, S. Qin, X. Yin, Photocatalytically reducing CO₂ to methyl formate in methanol over ZnS and Ni-doped ZnS photocatalysts, *Chem. Eng. J.* 230 (2013) 506–512.
- [37] K. Senthilkumar, T. Kalaivani, S. Kanagesan, V. Balasubramanian, J. Balakrishnan, Wurtzite ZnSe quantum dots: synthesis: characterization and PL properties, *J. Mater. Sci. Mater. Electron.* 24 (2013) 692–696.
- [38] N. Sasirekha, S.J.S. Basha, K. Shanthi, Photocatalytic performance of Ru doped anatase mounted on silica for reduction of carbon dioxide, *Appl. Catal. B Environ.* 62 (2006) 169–180.
- [39] T. Tan, D. Beydoun, R. Amal, Effects of organic hole scavengers on the photocatalytic reduction of selenium anions, *J. Photochem. Photobiol. A Chem.* 159 (2003) 273–280.